Chaos, Solitons and Fractals 163 (2022) 112556

Contents lists available at ScienceDirect

Chaos, Solitons and Fractals

journal homepage: www.elsevier.com/locate/chaos

An indicator to quantify the complexity of signals and surfaces based on scaling behaviors transcending fractal

Zhiwei Li [a,b], Jianjian Wang [b], Meng Yuan [a], Zhongyu Wang [a], Pingfa Feng [a,b], Feng Feng [a,*]

[a] Division of Advanced Manufacturing, Shenzhen International Graduate School, Tsinghua University, Shenzhen 518055, China
[b] Department of Mechanical Engineering, Tsinghua University, Beijing 100084, China

ARTICLE INFO

Keywords:
Roughness scaling characteristics
Fractal dimension
Complexity indicator
Hurst exponent
Weierstrass–Mandelbrot function
Milling vibration signals
Thin film surfaces

ABSTRACT

In the well-established fractal scheme, the fractal dimension (D) is a central indicator of the complexity of fractal features. The D values of non-fractal signals and surfaces are 1 and 2, respectively, while there can be varieties in their complexities. In this study, the scaling characteristics of root-mean-squared roughness could exhibit a continuous variation transcending the boundary between fractal and non-fractal by using the roughness scaling extraction (RSE) method proposed in previous study, and an universal indicator (H_{RSE}, Hurst exponent calculated by RSE method) to quantify the complexity of both fractal and non-fractal features is demonstrated. The actual signals (milling vibration) and surfaces (silver thin films) together with the artificial ones generated through Weierstrass–Mandelbrot (W–M) function were analyzed. Within the fractal scope, the calculated results with RSE method could be close to the ideal D values of W–M function with an accuracy higher than those of the traditional fractal methods (including Box-Counting, Higuchi, Katz, power spectral density, structure function, and autocorrelation function methods). For the non-fractal features, the complexity could also be quantified effectively by H_{RSE}. Chatter could be recognize by H_{RSE} of milling vibration signals, because it was larger than 1, from 0.5 to 1, and less than 0.5 in idling, stable milling and chatter milling states, respectively; For thin film surfaces, H_{RSE} increased monotonically from 0.79 to 1.32 along with Sq increasing, indicating a strong positive correlation. The findings indicated that the scaling analysis could be utilized for both fractal and non-fractal features, which would be beneficial for various engineering applications.

1. Introduction

Fractals have been widely applied in various fields, such as botany [1,2], biology [3,4], material [5] and hydromechanics [6,7] for decades since their introduction [8]. Fractals are regarded as an effective tool for studying the nonlinear and irregular geometry in mathematics and nature [9], and it is the most beautiful flower blooming from elementary mathematics and has a significant effect in engineering. Fractal dimension (D) is the core evaluation parameter of fractals [10,11] and could be used to evaluate the complexity of signals and surfaces in the fractal region. A fractal is a shape formed by parts similar to the whole in some way [9], indicating that the fractal has self-similarity and self-affinity properties. The multi-scale characteristics for surface roughness could be represented by fractal geometry because the actual surface has the self-affinity property [12,13]. The power-law relationship between surface roughness and D could be expressed: $Rq = AL^H = AL^{2-D}$, $Sq = AL^H = AL^{3-D}$, where Rq and Sq are the root mean square roughness of the profile and surface under scale L, respectively; A is the value of the root mean square roughness when $L = 1$; and H is the Hurst exponent. The multi-scale characteristic relationship between roughness and scale also exists for signals.

The irregularity and complexity of a waveform of time series could be quantified by the D, enabling its wide application in the signal analysis. For example, fractal analysis has been applied in the medical signals [14], such as accurately analyzing electroencephalography (EEG) signals for the automatic detection of epileptic seizures, obtaining authoritative diagnostic information for epilepsy [15], and electrocardiogram (ECG) data compression [16]. Fractal analysis also plays a significant role in machining vibration signals. Meanwhile, D could continuously monitor milling tool wear based on the vibration signals of the spindle [17], and monitor the processing state of the milling process. Thus, the chatter could be timely detected [18].

Fractal analysis is also widely adopted in surface topography. There are no perfectly smooth or flat surfaces, while most surfaces (such as engineering surfaces and thin films) are rather rough when viewed microscopically. Measurements on a variety of machined surfaces and thin films have shown that the surface topographies are multi-scale,

* Corresponding author.
E-mail address: feng.feng@sz.tsinghua.edu.cn (F. Feng).

https://doi.org/10.1016/j.chaos.2022.112556
Received 30 March 2022; Received in revised form 3 August 2022; Accepted 9 August 2022
Available online 27 August 2022

random, and hard to be measured. Nevertheless, D could characterize and simulate these rough surfaces [12]. D could characterize the regularity and fragmental property of machined surfaces [19], and it has great influences on the thermal contact conductance of two rough surfaces in contact. The surface topography of nanocomposite thin films could be characterized by D [20] and the domain walls [21–24]. There have been plenty of publications [12,19,20] where fractal theory was utilized to characterize and simulate rough surfaces by many groups. However, the actual surfaces could be significantly different from the theoretically fractal surfaces, because the fractal property can be applied to characterize or simulate an actual surface only within a certain extent of investigation scales, i.e. a scaling region. The necessity to consider the existence and influence of scaling region should also be noticed in the fractal analysis on both signals and surfaces.

The several commonly used methods for calculating D are as follows: the Box-Counting (BC) [25–27], Higuchi [28], and Katz [29] methods for signals; and power spectral density (PSD) [2,20,30], structure function (SF) [31], and autocorrelation function (ACF) [32] methods for surfaces. Over the past few years, a new method named roughness scaling extraction (RSE) was proposed to calculate D for signals [15,33] and surfaces [34]. The RSE method was found to be more accurate than the other methods in the fractal region. D ranges between 1 and 2 and 2 and 3 in terms of the dimensions of signals and surfaces, respectively. However, the calculated D is outside of this range, and the signals or surfaces are non-fractal, with an D of one and two, respectively [10]. However, the so-called non-fractal signal or surface often appears in previous literature and is thought to be miscalculated and hard to explain. These supposedly erroneous D need to be studied and explained for effectively characterizing signals and surfaces. It is worth noting that the features concerned in this study were surfaces and signals, while other cases such as Cantor set (the fractional dimension can be below 1) were not included in this study. Therefore, the non-fractal region referred to the cases when $D < 1$ for a signal and $D < 2$ for a surface.

In the previous study, the RSE method could accurately calculate the D not only of the fractal region but also of the non-fractal region, and the dimensional value continuously varied across the fractal and non-fractal profiles [33]. This method could also be used to distinguish the complexity of signals and surfaces. The values in the fractal region are D calculated by all methods. Meanwhile, the values in the non-fractal region could be defined as the indicator for complexity (H_{RSE}) calculated by the RSE method. The concept is expanded to include machining signals (milling vibration signals) and surface analysis (thin films), and the effect of flattening and planarization on the RSE method is demonstrated in this study. Evidence confirms that the roughness scaling characteristics could be summarized with continuity and saturability. Continuity means that the RSE method could theoretically restore the true input value in the fractal and non-fractal regions, indicating the corresponding complexity for real signals and surfaces. Saturability refers to the degree to which a calculation method could restore the input value of a fractal function. Continuity and saturability are of great significance to the complexity evaluation of signals and surfaces in the fractal and non-fractal regions.

The goal of this study is to propose an effective indicator to quantify the complexity of the signals and surfaces transcending the scope of fractal. H_{RSE} is the representative calculated values of RSE method in this study. Meanwhile, H_{RSE} is an indicator to quantify the complexity of both fractal and non-fractal features. H_{RSE} has a linear relationship with D_{RSE} (D calculated by the RSE method), $H_{\mathrm{RSE}} = 2 - D_{\mathrm{RSE}}$ (signals) and $H_{\mathrm{RSE}} = 3 - D_{\mathrm{RSE}}$ (surfaces), in the fractal region; H_{RSE} has no relationship with D_{RSE}, and D_{RSE} should be one and two for signals and surfaces, respectively, in the non-fractal region. In this study, the indicator for complexity of roughness scaling characteristics (H_{RSE}) was found to be ubiquitous in the fractal and non-fractal regions of signals and surfaces. A continuous variation of the scaling characteristics was observed across the fractal and non-fractal signals and surfaces, which could be characterized by using H_{RSE} values obtained with the RSE method. Meanwhile, the other fractal methods could not reflect the complexity of the non-fractal signals and surfaces. The H_{RSE} could effectively recognize chatter for milling vibration signals; For thin film surfaces, a strong positive correlation was between Sq and H_{RSE}. The RSE method has the potential to aid in the better understanding of nonlinear characteristics in a variety of research fields.

2. Methods and samples

2.1. Calculation methods

2.1.1. For signals

The BC, Higuchi, and Katz, and RSE methods were used to calculate the D and H_{RSE} of signals (the description of these methods are shown in Appendix A.1.1), respectively. The RSE method was based on the roughness method [35–37], which was one of the most effective methods at extracting the fractal properties. The scaling characteristics of roughness was of great significance in the studies in the fractal field [38–40]. There was an important procedure in RSE method named flattening, which could provide the capability of quantifying the complexity of non-fractal features and would be described below. Accordingly, the RSE method of the signals is divided into RSE-f0, RSE-f1, RSE-f2 and RSE-f3, which adopt zero-order polynomial (without flattening), first-order polynomial ($y_{f1} = ax + b$), second-order polynomial ($y_{f2} = ax^2 + bx + c$), and third-order polynomials ($y_{f3} = ax^3 + bx^2 + cx + d$) for flattening, respectively. The scaling region with a fixed slope was required because the $Rq-L$ curve was not always linear globally in the RSE method. In the $Rq - L$ curve, the deviation on the left (at smaller L) was the drop point, while that on the right (at larger L) was the corner point. The linear region of the curve between the drop and the corner points was the scaling region. The scaling region must be identified to improve the accuracy of the D calculation. Thus, the scaling region recognition method was used.

This method was based on the characteristics of the scaling region in the curve. First, a seventh-order polynomial $f(l)$ was used to fit the entire curve, and the fitting order n of the polynomial selected was an optimized empirical value. When n was larger, the fluctuation of the fitting curve was severe, compromising the subsequent segmentation of the curve according to the derivative size; whereas, when n was lower, the curve could not be properly fitted. Second, the first and second derivatives ($f'(l)$ and $f''(l)$) of $f(l)$ were obtained. Given the linearity of the scaling region, the corresponding $f'(l)$ should be a constant in the region, and $f''(l)$ should be zero. Accordingly, the scaling region was determined by the first condition of $|f''(l)| < \delta_1$. The series of l values in the region was marked as l_i and the corresponding $f'(l)$ values were averaged to obtain $\overline{f'(l_i)}$, which was the scope of the region. The second condition $|(f'(l) - \overline{f'(l_i)})/f'(l)| < \delta_2$ should also be considered because of the frequent fluctuations in the actual curves. L_i was the obtained and should be a continuous segment corresponding to the target scaling region in the $Rq - L$ curve. Meanwhile, L_i should be more than half of the total series; otherwise, the method was meaningless because the scaling region should represent the property of the global data. In a batch of data, the corresponding scaling region and parameters δ_1 and δ_2 should be fixed. $\delta_1 = 0.1$ and $\delta_2 = 0.85$ were used to determine the drop and corner points in the signals.

2.1.2. For surfaces

The PSD (including Jacobs method [2,30,41,42]), SF, and ACF, and RSE methods were used to calculate the D and H of the surfaces (the description are shown in Appendix A.1.2), respectively. The RSE method's surface processing could be divided into two types, flattening [34] and planarization [43]. The surface which the flattening process aims at is considered to consist of some profiles for the former. By contrast, the planarization process aims at the surfaces for the latter. In summary, the planarization processing was: $Z_x = Z - Z_{px}$, where Z

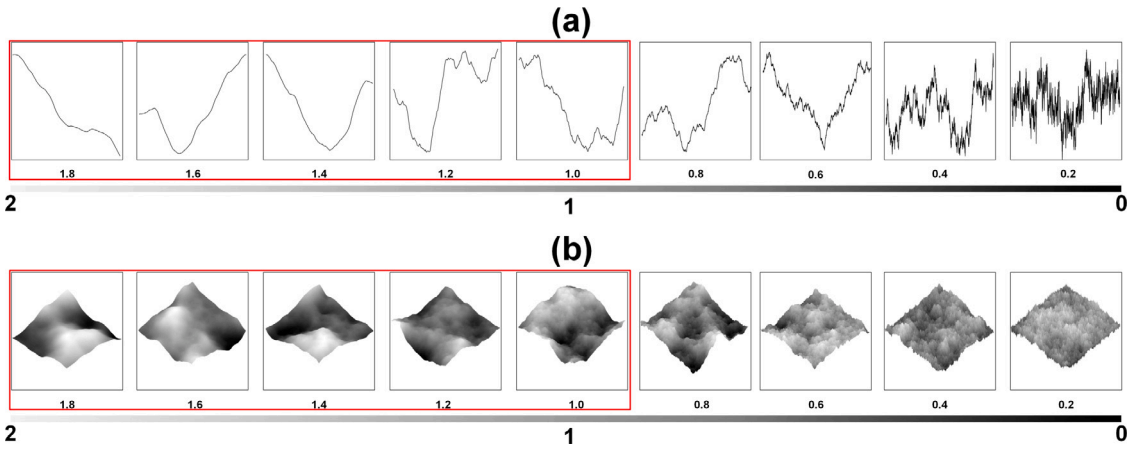

Fig. 1. The typical surfaces of artificial signals and surfaces generated through W–M function with H_i (a) values ranging from 1.8 to 0.2 by Eq. (1), (b) values ranging from 1.8 to 0.2 generated by Eq. (2), the sub-images from non-fractal region were surrounded by red boxes. (For interpretation of the references to color in this figure legend, the reader is referred to the web version of this article.)

was the original plane, Z_{px} was the plane with x-order planarization, and Z_x was the processed plane for calculation.

Accordingly, the RSE method for the surfaces was divided into flattening method (RSE-f0, RSE-f1, RSE-f2, and RSE-f3; the procedure was the same with signals) and planarization method (RSE-p0, RSE-p1, RSE-p2, and RSE-p3, which used zero-order without planarization; first-order planarization: $z_{p1} = A_1x + B_1y + C_1$, second-order planarization: $z_{p2} = A_2x^2 + B_2y^2 + C_2xy + D_2x + E_2y + F_2$, and third-order planarization: $z_{p3} = A_3x^3 + B_3y^3 + C_3xy^2 + D_3y^3 + E_3x^2 + F_3xy + G_3y^2 + H_3x + I_3y + J_3$, respectively). The same scaling region recognition method ($\delta_1 = 0.15$, $\delta_2 = 1$) was used to identify the scaling region for the $Sq - L$ curve of surfaces.

2.2. Samples

2.2.1. Artificial samples

Fractal analysis requires the use of fractal functions to investigate the properties of the calculation method. These functions are continuous and non-differentiable everywhere [44]. Examples of the commonly used fractal functions are the W–M [12,33,45–51], Takagi [52,53], and Fractional Brownian functions [54,55]. The W–M function has been extensively investigated by previous studies and has been widely used in various fields. Eqs. (1) and (2) are the 1D and 2D forms of W–M function, respectively. All the artificial signals and surfaces are of 1024 points generated by Eq. (1) and of 512 × 512 points generated by Eq. (2). Matlab and Python were used for calculation to estimate the D and H_{RSE}. The W–M function was used to describe fractal signals, as shown in Eq. (1). This function could also be used to describe fractal surfaces, as shown in Eq. (2).

In Eq. (1), D is the ideal dimensional value of the generated signals that ranged from one to two for D; n is a frequency index; ϕ_n is a random phase for preventing the coincidence of different frequencies at any points of the signal; γ is a parameter that used to determine the density of frequencies in the signals, $\gamma = 1.5$; and M is the number of overlapping components, $M = 200$. In Eq. (2), D ranges from two to three for D; L is the length of the surface, $L = 80$ μm; G is the fractal roughness, $G = 0.2 \times 10^{-3}$ μm; γ is the density of frequencies in the profile, $\gamma = 1.5$; M is the number of superposed ridges, $M = 10$; L_s is the cut-off length, $L_s = 2 \times 10^{-3}$ μm; ϕ_{mn} is the homogeneously distributed random phase shift; and n_{max} is the upper limit of n, $n_{max} = int[log(L/L_s)/log((\gamma))]$, where $int[...]$ denotes the maximum integer value of the number in the brackets.

$$z(x) = \sum_{n=0}^{M} \gamma^{(D-2)n} \left[\cos \phi_n - \cos(\gamma^n x + \phi_n) \right] \tag{1}$$

$$z(x,y) = L\left(\frac{G}{L}\right)^{D-2}\left(\frac{l n \gamma}{M}\right)^{\frac{1}{2}} \sum_{m=1}^{M}\sum_{n=0}^{n_{max}} \gamma^{(D-3)n} \times \left\{ cos\phi_{mn} - cos\left[\frac{2\pi\gamma^n(x^2+y^2)^{\frac{1}{2}}}{L} cos\left(tan^{-1}\frac{y}{x} - \frac{\pi m}{M}\right) + \phi_{mn}\right] \right\} \tag{2}$$

In Eq. (1), we define: $H_i = 2 - D_i$; while in Eq. (2), we define: $H_i = 2 - D_i$. Several non-fractal and fractal signals were generated as artificial signals by using Eq. (1), where H_i ranged from 1.8 to 0.2 spaced equally. Nine sub-images represent the inputting H_i from left to right and non-fractal to fractal. Fig. 1(a) shows that the fractal signals are more complex, and the smaller H_i from the non-fractal region corresponds to the more complex signals. The typical surfaces of artificial surfaces were generated by using Eq. (2) with H_i ranging from 1.8 to 0.2 spaced equally. Nine sub-surfaces also represent the inputting H_i from left to right and from non-fractal to fractal. Fig. 1(b) shows that the fractal surfaces are more complex, and the smaller H_i from the non-fractal region also corresponds to the more complex surfaces.

2.2.2. Actual samples

The RSE-f2 of the signals and the RSE-p2 of the surfaces were used to determine the H_{RSE} of the actual samples to be consistent with previous studies. Continuous variations across the fractal and non-fractal regions were also found for the actual signals and surfaces. The scaling region recognition method is used, as shown in Fig. 2. Fig. 2(a) and (b) illustrate the typical $Rq - L$ curves with a signal sample length of 1000 points. Fig. 2(c) and (d) illustrate the typical $Sq - L$ curves with a surface sample range of 512 × 512 points. The H_{RSE} values of Fig. 2(a), (b), (c), and (d) are 0.896, 1.664, 1.352 and 0.889, respectively. The drop values of the signals were all quite low and rarely existed, whereas the corner values were approximately 100 and appeared in most signals. The corner values of surfaces had a large fluctuation, ranging from 100 to 500.

The first series of actual signals noted in this work were the milling vibration signals of a numerical control machine tool, which was used in chatter recognition [18,56–62]. The method of obtaining the signals is shown in Appendix A.2.1. The signals are illustrated in Fig. 3(a), nine sub-images represent the H_{RSE} from left to right and from non-fractal to fractal. The fractal signals are more complex. The smaller H_{RSE} from the non-fractal region corresponds to the more complex signals. The H_{RSE} values of the signals could continuously vary across one, indicating the existence of continuous variation across the fractal and non-fractal regions.

The second series of actual surfaces were the surface morphology of silver thin films, which were used in many fields, such as optical engineering [63] and superconductor sample fabrication. The magnetron

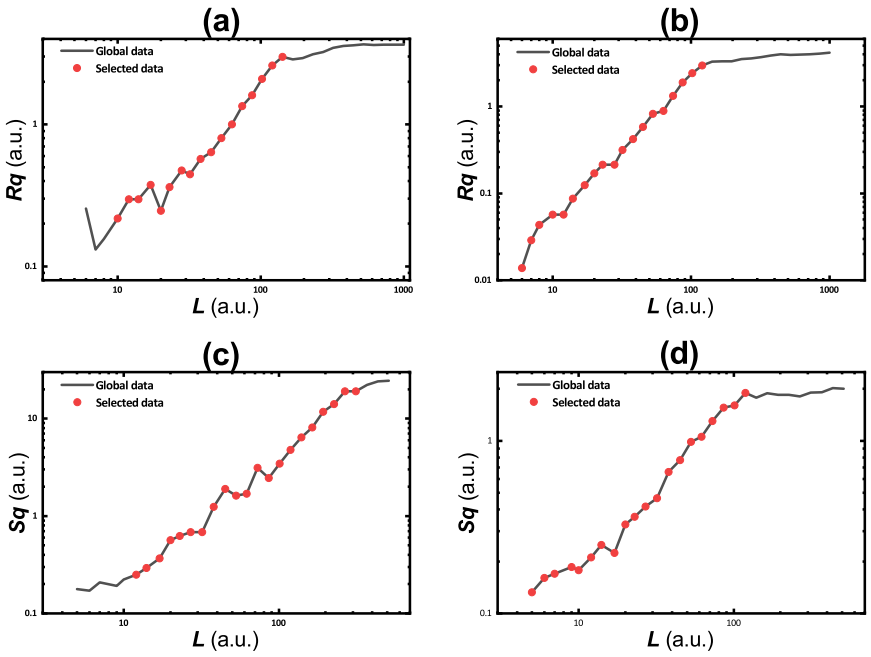

Fig. 2. The typical $Rq - L$ curves obtained by H_{RSE} (a) 0.896 (b) 1.664 with signal sample length of 1000, $Sq - L$ curves by H_{RSE} (c) 1.352 (d) 0.889 with surface sample range of 512 × 512. The scaling regions obtained by the recognition method were plotted by using red circle symbols.

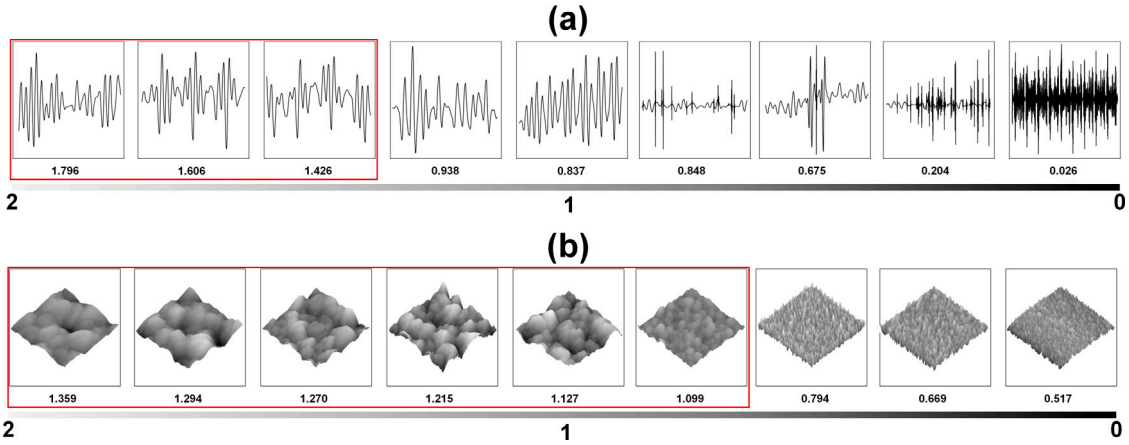

Fig. 3. The typical images of real signals and surfaces obtained by (a) vibration signals from milling, H_{RSE} ranging from 1.796 to 0.026, (b) thin films deposited via magnetron sputtering, H_{RSE} values ranging from 1.359 to 0.517.

sputtering process and the material are described in Appendix A.2.2, atomic force microscopy (AFM) was employed to measure the surface as in the previous literature [64–66]. The surfaces are illustrated in Fig. 3(b). The nine sub-images represent the H_{RSE} from left to right and from non-fractal to fractal. The fractal surfaces are more complex, and the smaller H_{RSE} from the non-fractal region corresponds to the more complex surfaces. The H_{RSE} values of the surface could also continuously vary across one.

Based on the above, the continuity existed in the actual signals and surfaces by using the RSE method. The results showed that the H_{RSE} was larger than zero. Saturability could be observed in the actual signals and surfaces. The continuity and saturability illustrated the characteristic of the RSE method to quantify the complexity in the actual calculation (whether signals or surfaces). The milling vibration signals and silver thin films were used to recognize chatter and investigate the relationship between Sq, H_{RSE}, and T. The evidence from the actual signals and surfaces could illustrate the indicator for complexity of roughness scaling characteristics.

3. Results and discussion

3.1. Chatter recognition

Chatter is a complex self-excited vibration, and its vibration signal is nonlinear and nonstationary, which has a significant negative effect on the surface quality [58]. In recent years, a variety of methods have been proposed to identify and suppress chatter and achieved good results [18,56,57,59–62]. The D is considered to be able to timely and effectively detect chatter and is important in improving the surface quality [18]. Accordingly, the D was used to recognize chatter on the basis of the RSE method. The analysis of stable and chatter vibration signals is illustrated in Fig. 4. The overall signals are demonstrated in Fig. 4(a) and (b), and the corresponding H_{RSE} and D_c results calculated by using the RSE-f2, Higuchi, and BC methods are presented in Fig. 4(c) and (d), respectively. The fast Fourier transform (FFT) results are shown in Fig. 4(e) and (f). The length of vibration signals was 10.15625 s, 130,000 points, and the milling process was started at 1.63 s and ended at 8.93 s. One line from Fig. 4(c) and (d) is consisted of 130 points

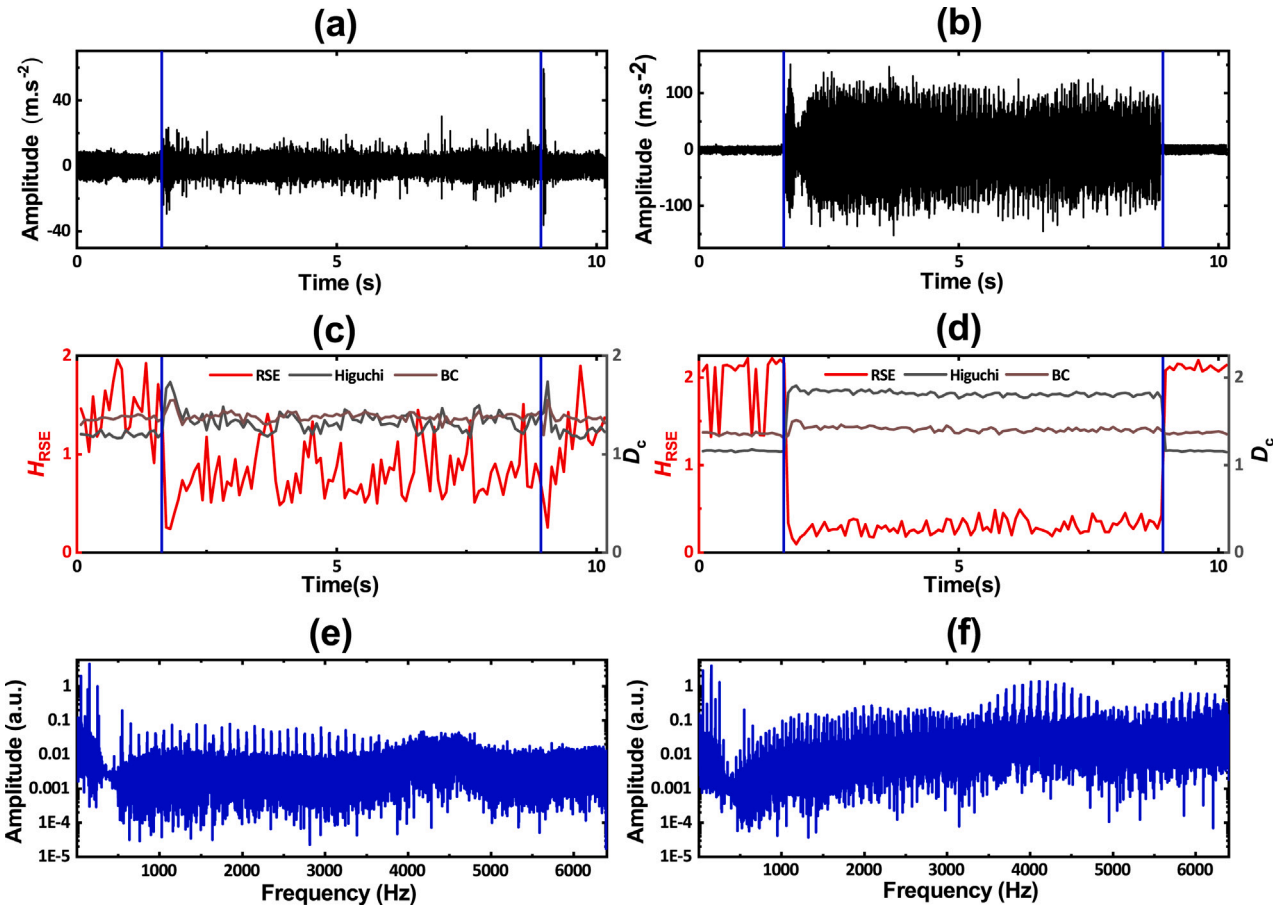

Fig. 4. Milling vibration signals, the corresponding H_{RSE}, D_c, and FFT results of the stable state: (a), (c), (e) and chatter state: (b), (d), (f), respectively. The FFT results were calculated under milling process between the two blue lines. (For interpretation of the references to color in this figure legend, the reader is referred to the web version of this article.)

(0.01 s), one point of the line was calculated using 1000 signal points. As shown in Fig. 4(c) and (d), the H_{RSE} could continuously change below or above one (i.e., across the fractal and non-fractal regions, respectively). The FFT results from Fig. 4(e) and (f) showed that the signal frequency sources were more extensive in chatter state.

The stable signals show that the fluctuation range of the vibration signals was from -20 m s^{-2} to 20 m s^{-2}, the vibration was slight, and the quality of the actual processed surface was great. The approximate range of the H_{RSE} was from 0.5 to 2. The H_{RSE} ranged from 1 to 2 and 0.5 to 1 in the idling and milling processes, respectively, indicating that the H_{RSE} could distinguish the unmachined and machined states. The main difference from the H_{RSE}s was that the signals of the unmachined and machined states had varying complexity. The complexity of the signals of the idling process was low. By contrast, the complexity of the milling process was relatively high and the corresponding H_{RSE} could be less than 1. Meanwhile, the D_cs calculated by using the Higuchi and BC methods were slightly changed in the idling and milling processes.

The feed rate was the same for stable and chatter milling, and the experiment setup was not changed for the chatter signals. The fluctuation range of the signals was from -100 m s^{-2} to 100 m s^{-2}. The vibration was particularly strong in the chatter milling that the actual processed surface quality was poor. The approximate range of the H_{RSE} was from 0 to 2.2, and those in the idling and milling processes ranged from 1 to 2.2 and 0 to 0.5, respectively. In comparison with the H_{RSE}, the D_cs calculated by using the Higuchi method were also greatly changed between the stable and the chatter states, but BC method was not.

The vibration of the chatter signals is more intense, and the amplitude is higher compared with the stable signals, as shown in Fig. 4(b). The more complex the signals, the larger the D_c. The comparison results of the H_{RSE} of the stable and chatter signals and other methods are as follows: 1. The H_{RSE} could recognize the idling and milling processes; the corresponding H_{RSE} of the idling state was between 1 and 2, and that of the milling state was less than 1; 2. The H_{RSE} was more than 0.5 and less than 0.5 in the stable and chatter signals, respectively, which could help effectively recognizing chatter. Therefore, $H_{RSE} = 0.5$ was the boundary between the stable and the chatter signals.

Based on the above, the H_{RSE} could recognize effectively chatter. The H_{RSE} could be larger than zero, and saturability could be observed in the vibration signals. The H_{RSE} was larger than 1, from 0.5 to 1, and less than 0.5 in the idling, stable, and chatter processes, respectively. Continuity could also observed in the vibration signals. Meanwhile, non-fractal signals ($H_{RSE} > 1$) meant idling process, low complexity; while fractal signals ($H_{RSE} < 1$) meant milling process, high complexity. The condition of $H_{RSE} = 0.5$ could effectively distinguish the actual milling state: $H_{RSE} > 0.5$, stable; $H_{RSE} < 0.5$, chatter. The example of chatter recognition illustrated the advantage of the transcending H_{RSE} in the actual signal calculation.

3.2. Magnetron sputtering deposition

The typical surface morphologies of silver thin films measured by AFM is shown in Fig. 5. The substrate temperatures are 25 °C of Fig. 5(a) and (b), 100 °C of Fig. 5(c) and (d), 200 °C of Fig. 5(e), 300 °C of Fig. 5(f) and (g) and 400 °C of Fig. 5(h) and (i). The Sq values of the samples are 2.08, 2.02, 6.70, 7.08, 23.82, 33.74, 39. 73, 51.20, and 41.08 nm with the H_{RSE} of 0.52, 0.67, 1.10, 1.11, 1.22, 1.23, 1.26, 1.34, and 1.36, which are denoted from Fig. 5(a) to (i), respectively.

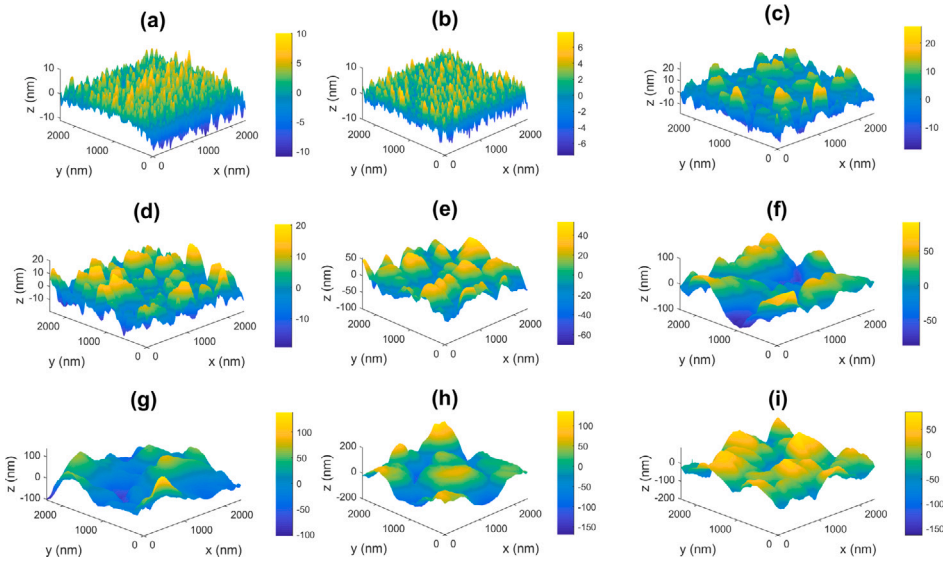

Fig. 5. Typical surface morphologies of silver thin films with a substrate temperature, 25 °C: (a) (b), 100 °C: (c) (d), 200 °C: (e), 300 °C: (f) (g), and 400 °C: (h) (i).

The Sq and H_{RSE} increased with the temperature increase. Fig. 5 shows that the surface clusters of the film at the same measurement scale gradually expand with the rise in substrate temperature. At room temperature (25 °C), the number of clusters on the surface of the film at 2.4 μm × 2.4 μm could not be directly measured, and the surface morphology was complex and broken. However, at 400 °C, the number of clusters on the surface of the film at this scale was countable with only a few clusters, and the overall surface morphology was flat and simple. In addition, new small clusters formed on the clusters at higher temperature. Therefore, silver atoms were more likely to form larger grains or clusters in the process of sputtering deposition with the rise in substrate temperature. Meanwhile, the Sq and H_{RSE} of the thin films were highly positive correlated.

The relationship of the Sq, H_{RSE}, D_c, and H_c calculated by using the AFM data for the silver thin films with T ranging from 25 °C to 400 °C is explored for investigating the influence of surface morphology in magnetron sputtering, as shown in Fig. 6. A strong correlation is observed among Sq, H_{RSE} and T. Sq monotonically increased from 2.08 nm to 41.12 nm when H_{RSE} increased fro 0.79 to 1.32 with T increasing from 25 °C to 400 °C. Sq increased with the increase in the substrate temperature. However, the D_c and H_c calculated by PSD had no obvious changes. As previously mentioned, the higher the base temperature was, the larger the grains formed by the silver atoms in the deposition process would be, and even clusters would be formed at the end. The larger grain size would cause the surface of the silver film to be more undulated and show a larger global roughness. The grain size could be reflected by H_{RSE}. The results also implied that a strong positive correlation between Sq and H_{RSE}, which was consistent with previous studies on the fractal analysis of various surfaces.

From the above, the H_{RSE} was an effective measuring index of surface complexity and could characterize the change of surface morphology. Sq increased with the increase in the substrate temperature, while the grain size of the silver thin films increased. Meanwhile, the number of grains in the same sample within the same measurement scale decreased. Accordingly, the complexity and density of silver thin films also decreased. H_{RSE}, as a variable to measure the complexity and fragmentation of surface morphology, would also increase, as shown in Fig. 3(b) (from right to left). The artificial signals and surfaces generated by the W–M function of larger intervals in comparison with other methods were studied to further investigate the unique characteristic (from non-fractal to fractal) of H_{RSE}.

3.3. Artificial signals and surfaces

Fig. 7(a) demonstrates that the H_{RSE} could match with D_i within a large scope (RSE-f1 matched from 0 to 2, RSE-f2 matched from 0 to 3 and RSE-f3 matched from 0 to 4), except for the RSE-f0 method, by using the D_i values ranging from −2.5 to 2. However, the Higuchi method was effective only in the fractal region (from 1 to 2), and the accuracy was lower than that of the RSE method. Two other methods, BC and Katz, had the lowest accuracy in the fractal region, as shown in Fig. 7(b). Almost all the other methods could not reflect the variation of the signal's complexity in the non-fractal region (D_i below one). Such a phenomenon was also an implication that the D of a non-fractal signal was theoretically one [33]. Therefore, the RSE method was suitable in characterizing the continuous variations of the signal's complexity across the fractal and non-fractal regions, while the other methods were not.

The RSE method has a better continuity than the other methods in the fractal region (D_i ranges from 1 to 2) and non-fractal region (D_i less than one) in terms of signals, as shown in Fig. 7. The aforementioned method could restore the true input value (H_{RSE} matched with D_i, $H_{RSE} = 2 - D_i$) at a certain extent. All calculation methods had saturability, and the other methods were less saturated. However, the saturability of the RSE method was gradually increased with the increasing of the order of flattening. The generated signal is essentially a discretization of a function (Eq. (1)) that is continuous everywhere. Accordingly, H_{RSE} should be larger than zero and all H_{RSE} should saturate at zero. Therefore, the RSE method had a better saturability. The H_{RSE} calculated by RSE-f2 based on signals was used in the previous calculation of the vibration signals, together with the accuracy, continuity, and saturability.

The artificial surfaces are also evaluated by using the RSE (flattening and planarization) and the other methods (PSD, SF and ACF), as shown in Fig. 8. Fig. 8(a) shows that the H_{RSE} could match with D_i within a large scope (the RSE-f1 matched from 0 to 2, the RSE-f2 matched from 0 to 3, and the RSE-f3 matched from 0 to 4), except for the RSE-f0 method, by using D_i values ranging form −1.5 to 3. The results of the RSE method based on the planarization is the same as flattening, as shown in Fig. 8(b). However, the SF method is effective only in the fractal region (D_i ranges from 2 to 3), where its accuracy is lower than that of the RSE method. Two other methods, PSD and ACF, have the lowest accuracy in the fractal region, as shown in Fig. 8(c). Almost all the other methods could not reflect the variation of signal complexity in the non-fractal region (D_i below two). Such a phenomenon was also

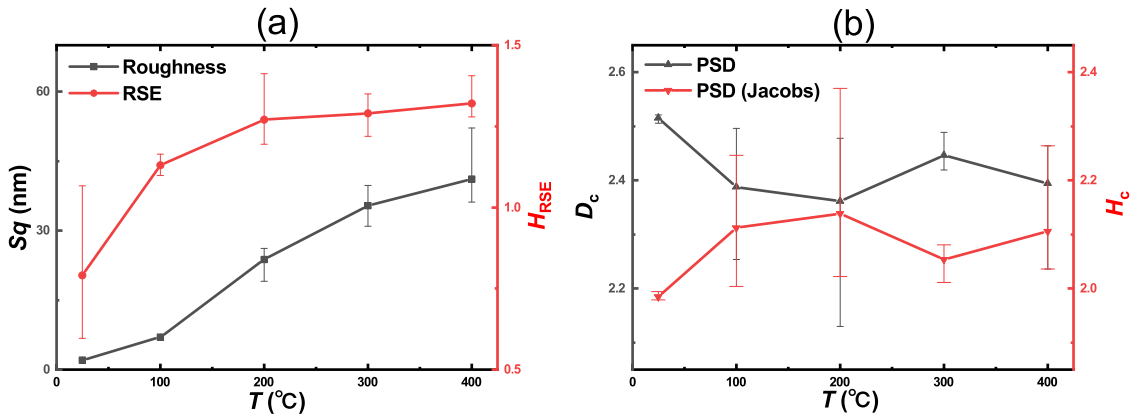

Fig. 6. For the silver thin films deposited with substrate temperature ranging from 25 °C to 400 °C, (a) Sq and H_{RSE} calculated with RSE-p2 method, (b) D_c and H_c calculated with PSD method. For each data-point, the total number of measurements was five.

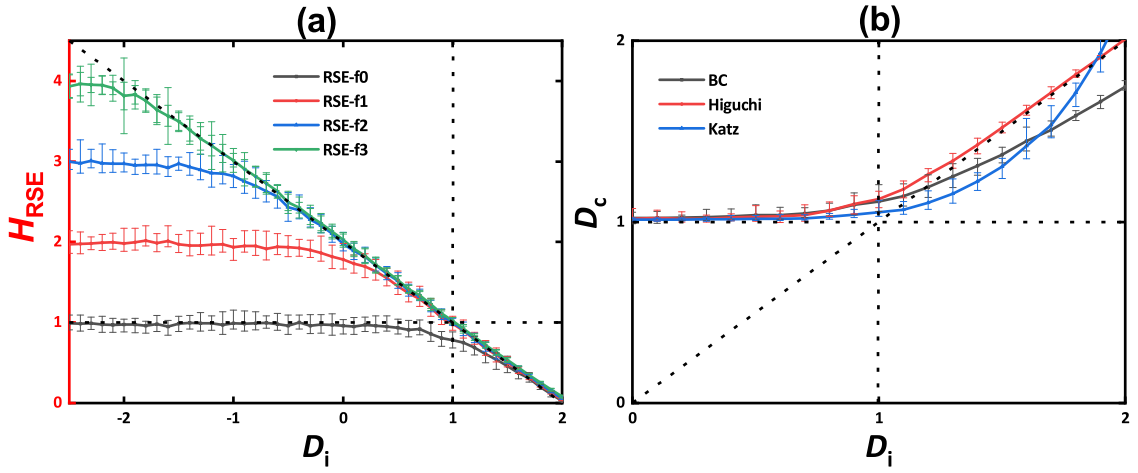

Fig. 7. Comparison of (a) the H_{RSE} of RSE-f0, RSE-f1, RSE-f2, and RSE-f3 methods, (b) the D_c of BC, Higuchi, and Katz methods generated through W–M function with D_i ranging from −2.5 to 2 generated by Eq. (1).

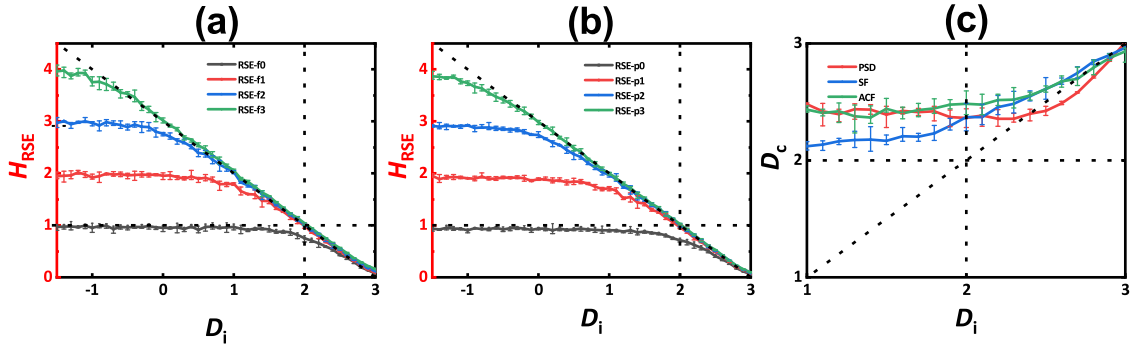

Fig. 8. Comparison of (a) the H_{RSE} of RSE-f0, RSE-f1, RSE-f2, and RSE-f3 methods, (a) the H_{RSE} of RSE-p0, RSE-p1, RSE-p2, and RSE-p3 methods, (c) the D_c of PSD, SF, and ACF methods for the surfaces generated through W–M function with D_i ranging from −1.5 to 3 generated by Eq. (2).

an implication that D of a non-fractal surface was theoretically two. Therefore, the RSE method (flattening and planarization) was suitable in characterizing the continuous variations of the surface complexity across fractal and non-fractal regions, whereas the other methods were not.

In terms of surfaces, the results from Fig. 8 show that the RSE method has a better accuracy, continuity, and saturability than the other methods in the fractal region ($2 < D_i < 3$) and non-fractal region ($D_i < 2$). The RSE method could restore the true input value at a certain extent. All calculation methods had saturability, while the other methods were less saturated. The saturability of the RSE method gradually increased with the increase of the flattening order. The artificial surface is essentially a discretization of a function (Eq. (2)) that is continuous everywhere. Therefore, H_{RSE} should be larger than zero, and all H_{RSE} should saturate at zero. Based on the above, the RSE method had a better saturability. The H_{RSE} calculated by RSE-p2 based on surfaces was used in the previous calculation of the thin films, together with the accuracy, continuity, and saturability of the calculation results.

3.4. Discussion

This study aims to quantify the complexity of the signals and surfaces by using the RSE method. A continuous variation of the dimensional value calculated with the RSE method (H_{RSE}) was observed across the fractal and non-fractal signals and surfaces based on the roughness scaling characteristics, while the other methods were not. The evidence from the actual (milling vibration signals and silver thin films) and artificial (generated through the W–M function) signals and surfaces showed that the H_{RSE} could effectively quantify the complexity of the signals and surfaces, such as chatter recognition and surface morphology measurement, indicating that the RSE method could potentially aid in the better understandings of the nonlinear behaviors and could be applied in various research fields. Therefore, H_{RSE} could be used as an indicator for complexity on the fractal and non-fractal features.

Vibration signals are regarded as the main assessment basis for chatter recognition, and D is commonly used to measure the signals. Previous studies mainly used D as an auxiliary judgement [18,67], the main drawback was that the results of the D calculation were slightly different in the chatter and stable states, e.g. the calculated D variation for different processing stages could be even less than 0.5, which was not convenient for practical application. According to the investigation of the roughness scaling characteristics, the optimized RSE algorithm could greatly improve the recognition accuracy. The H_{RSE} under different states widely varied and could accurately determine the corresponding machining processing state, and the actual application is convenient, as shown in Fig. 4. In addition, the H_{RSE} calculated by the RSE method could quantitatively express different processing states, and specific calculated values correspond to certain processes, which is a key application in the future and needs further investigation. Meanwhile, the Higuchi method also had an excellent performance in recognizing chatter, which also requires further investigation in the future. Recently, it has been reported that the use of multifractal analysis to study chatter can also achieve good results, which can accurately compare and identify vibration signals in different states and have a large degree of discrimination [68,69]. Thus a comparative study on the functionality of both H_{RSE} and multifractal analysis will be carried out in the successive study.

The technique of depositing silver materials on the silicon substrates to form thin films with special properties has been used. The deposition is always accompanied by a variety of complex physical and chemical processes under non-equilibrium conditions. In the process, silver atoms are continuously deposited on the silicon substrates, forming clusters and multi-scale self-similar structures, which can be measured by the fractal process. As shown in Fig. 5, the surface morphologies of silver films at different temperatures were significantly different, which could be illustrated by Sq. The H_{RSE} values could efficiently measure the change in surface topography, revealing the influence of substrate temperature in silver thin film deposition via magnetron sputtering. Thus the H_{RSE} curve meets the positive correlation with the Sq one, as shown in Fig. 6(a). However, the results calculated by PSD method is not satisfactory as shown in Fig. 6(b), unlike the previous studies on fractal studies [2,23,41]. Such a difference might be attributed to the variation across fractal and non-fractal within the research scope of this study. Besides, due to the difference in definitions of the power law relationship, D_c and H_c exhibit a linear relationship: $D_c = 4.5 - H_c$. More signals and engineering surfaces need to be studied in the future to further illustrate the unique complexity measurement function of H_{RSE} in the signal analysis and surface topography.

The concepts of roughness scaling characteristics, including continuity and saturability, to expand the application range were proposed by optimizing the RSE method and investigating the W–M function. In this study, the D_c calculated by each method have their own connotation, and they could be either fractal or non-fractal, indicating the complexity of the corresponding objects (signals and surfaces). The RSE method has the advantages of higher computational accuracy, better continuity and larger saturability according to a series of artificial signals and surfaces generated by the W–M function, as shown in Figs. 7 and 8. The flattening orders are the only variation in the RSE method. In previous studies [34,43], the processing order was used because the measured sample might be inclined or curved. Accordingly, the first-order or second-order polynomial was needed for processing. However, the higher flattening order could not only enhance the smoothness of the original data but also reduce the low frequency information of the original data. Therefore, higher-order polynomial processing, such as three, was also adopted.

The higher the order of flattening, the larger the range of calculation for signals. Under the same processing method, the higher the order, the larger the calculation range for surfaces. In this study, the highest order was only given to three. Although the calculation range might be increased by using a higher flattening order, which could be inferred based on the results of Figs. 7 and 8, the essence of processing is to utilize curves or surfaces of a specific order to fit the original data. The fitted data are subtracted out of the original data to obtain the processed data. A discrete curve consisting of n points, $n-1$ polynomials, can completely fit the curve. Accordingly, the $n-1$ degree polynomials can completely fit signals or surfaces composed of n points. Specifically, the processed data would be meaningless (all zeros) depending on the size of the original data when the processing order of the RSE method is large enough. Based on the above, the computation range of the RSE method only increases with the increase in the processing order to a certain extent. Although the larger processing order could help in extending the range of the H_{RSE}, the computational time would greatly increase, which is detrimental to the application. Meanwhile, the approaches of signal filtering and fitting by using sinusoidal instead of polynomials were also attempted for flattening. However, the results of such approaches were worse than the flattening by using polynomials. Thus, the mechanisms of information reduction would be studied in our future research to further analyze the RSE method.

Based on the above findings of this study, H_{RSE} could be regarded as an indicator for complexity because it could represent fractal and non-fractal regions and could provide the corresponding meanings in practical application, which allows it to be applied to more signals, such as electroencephalograph (EEG) signals, as well as more surfaces, such as machined surfaces. The artificial neural network (ANN) [70] and multifractal analysis [68,69,71] would be applied to rapidly obtain the dimension in our future work for practical approaching in engineering applications based on the feasibility demonstration of complexity quantification by using the H_{RSE}.

4. Conclusion

In this study, the indicator for complexity of roughness scaling characteristics was found to be ubiquitous in the fractal and non-fractal regions of signals and surfaces. A continuous variation of the scaling characteristics was observed across the fractal and non-fractal signals and surfaces, which could be characterized by using H_{RSE} values obtained with the RSE method. H_{RSE} could effectively recognize chatter for milling vibration signals and characterize the change of surface morphology, thus the application of H_{RSE} could be helpful and promising in various fields including surface science and manufacturing technology. Meanwhile, the other fractal methods could not reflect the complexity of the non-fractal signals and surfaces. The RSE method has the potential to aid in the better understanding of nonlinear characteristics in a variety of research fields. The conclusions reached are as follows: The continuous variation of roughness scaling characteristics was found in actual milling vibration signals and silver thin film surfaces, indicating that such a phenomenon and the indicator for complexity might extensively exist. Therefore, the H_{RSE} could be called the indicator for complexity for its ability on indicating complexity. H_{RSE} could effectively recognize chatter for milling vibration signals.

The H_{RSE} was larger than 1, from 0.5 to 1, and less than 0.5, in the idling, stable milling, and chatter milling processes, respectively. $H_{RSE} = 0.5$ was the boundary between the stable and the chatter states. H_{RSE} was an indicator for surface complexity and could characterize the change of surface morphology. Sq monotonically increased from 2.08 nm to 41.12 nm while H_{RSE} increased from 0.79 to 1.32 with T increasing from 25 °C to 400 °C, indicating a strong positive correlation between Sq and H_{RSE}. The saturability of the signals and surfaces were obtained under different processing orders by quantifying the W–M function. In brief, zero and processing order plus one are the lower and upper limits of saturability, respectively.

CRediT authorship contribution statement

Zhiwei Li: Methodology, Software, Writing – original draft. **Jianjian Wang:** Investigation, Writing – review & editing, Supervision. **Meng Yuan:** Validation, Resources, Data curation. **Zhongyu Wang:** Data curation, Writing – review & editing. **Pingfa Feng:** Writing – review & editing, Project administration. **Feng Feng:** Conceptualization, Methodology, Writing – review & editing.

Declaration of competing interest

The authors declare that they have no known competing financial interests or personal relationships that could have appeared to influence the work reported in this paper.

Data availability

Data will be made available on request.

Acknowledgments

This study was supported by National Natural Science Foundation of China under Grant No. 51875311, Guangdong Basic and Applied Basic Research Foundation under Grant No. 2020A1515011199, and Shenzhen Foundational Research Project under Grant No. WDZC20200817152115001. The authors would like to thank Yousheng Xia for his efforts to propose the scaling region algorithm and Junlong Huang for his efforts in the silver thin films deposition.

Appendix. Methods and samples

A.1. Calculation methods

A.1.1. Methods for signals

BC method:

BC method is one of the most widely used calculation method. The minimum number of boxes with a length of L covering the whole signal is N. When L approaches 0, there is a relationship depending on D:

$$N \propto L^{-D} \tag{A.1}$$

$$\ln N \propto -D \ln L \tag{A.2}$$

Fitted in double logarithmic coordinates, D is the opposite slope of the curve.

Higuchi method:

Higuchi method has the better calculation accuracy. It is a calculation method based on the length measurement of signal $L(k)$. Taking k sampling points as the unit, D satisfies:

$$L(k) \propto k^{-D} \tag{A.3}$$

For signal $X = x(1), x(2), x(3), \ldots, x(N)$, $k = k_{min}, \ldots, k_{max}$, rebuild k new time series: $X_k^m = x(m), x(m+k), x(m+2k), \ldots, x(m + \lfloor \frac{N-m}{k} \rfloor \cdot k)$, $m = 1, 2, 3, \ldots, k$, among them: m is the initial point, k is the interval, $\lfloor\ \rfloor$ denotes the Gauss' notation and both m and k are integers. For k reconstructed new sequences, calculate the length of each sequence $L_m(k)$:

$$L_m(k) = \frac{1}{k}\left(\sum_{i=1}^{\lfloor (N-m)/k \rfloor} | x(m+ik) - x[m+(i-1)k] |\right)\frac{N-1}{\lfloor (N-m)/k \rfloor k} \tag{A.4}$$

N is the total number of signal, and $\frac{N-1}{\lfloor (N-m)/k \rfloor k}$ is the normalization correction factor. Take the average length of k sequences with the same interval as the signal length $L(k)$ corresponding to interval k, namely:

$$L(k) = \frac{1}{k}\sum_{m=1}^{k} L_m(k) \tag{A.5}$$

$$\ln L(k) \propto -D \ln k \tag{A.6}$$

Given that each signal series $X(k)$ and the corresponding series length $L(k)$, fitted in the double logarithmic coordinates, D is the opposite slope of the curve.

Katz method:

Katz method is another important method. Assuming that the signal is made up of a series of data points (x_i, y_i), $i = 1, 2, 3, \ldots, N$, then the dimension of Katz method is defined as follows:

$$d = max\left(\sqrt{(x_i - x_1)^2 + (y_i - y_1)^2}\right) \tag{A.7}$$

$$L = \sum_{i=1}^{N-1}\left(\sqrt{(x_{i+1} - x_i)^2 + (y_{i+1} - y_i)^2}\right) \tag{A.8}$$

$$D = \frac{\log(n)}{\log(n) + \log(\frac{d}{L})} \tag{A.9}$$

n refers to the number of intervals between adjacent points ($n = N - 1$), and r refers to the diameter range (i.e., the maximum distance from the first point of the signal to any other point) maximum plane of the signal, L refers to the length of the signal.

RSE method:

RSE method has the best calculation accuracy. The roughness Rq and the data point length L satisfy:

$$Rq = AL^H = AL^{2-D} \tag{A.10}$$

Among this, A: Rq value when $L = 1$; H: Hurst exponent ($0 < H < 1$, in the fractal region); D: fractal dimension ($D = 2 - H$). The Rq and L of the fractal curve satisfy the above equation, and D can be obtained by fitting a straight line to them in the double logarithmic coordinate system:

$$\ln Rq = H \ln L + \ln A = (2 - D)\ln L + \ln A \tag{A.11}$$

A.1.2. Methods for surfaces

PSD method:

PSD method is based on the assumption that fractal surface morphology is superimposed by the infinite frequency mode. If $y(x)$ is the height sequence representing one of the surface signals, its Fourier transform and power spectrum in the range of length L are:

$$z(\omega) = \int_0^l y(x)e^{-j\omega x}\,dx \tag{A.12}$$

$$P(\omega) = \frac{|z(\omega)|^2}{l} \tag{A.13}$$

The relationship of power spectrum density $S(\omega)$ and the corresponding frequency ω depends on D:

$$S(\omega) \propto \omega^{-(5-2D)} \tag{A.14}$$

Given that each $S(\omega)$ and the corresponding frequency ω, fitted in the double logarithmic coordinates, K is the of the slope of the curve,

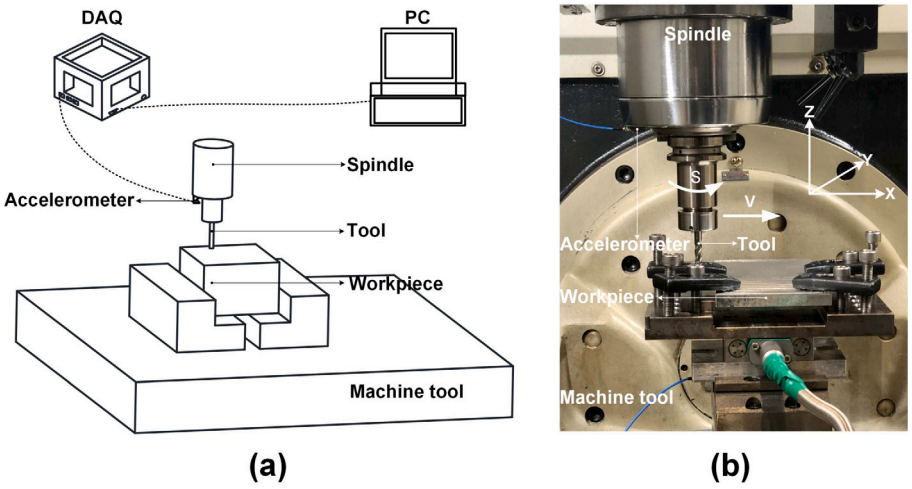

Fig. A.1. Experiment setup: (a) schematic diagram (b) photo of the experiment setup.

thus $D = (5 + K)/2, -3 < K < -1$. Calculating all dimensions of the signals to get mean value $\overline{D}$, the dimension of the surface is $D_p = \overline{D} + 1$.

PSD method (Jacobs):

For Hurst component (H), to analyze the AFM images, the one-dimensional PSD was obtained for different scan lines and the average PSD was estimated by Jacobs:

$$\mathrm{PSD}^{1\mathrm{d}}(q_x) = L_x^{-1}\left[\int_{L_x} h(x,y)e^{-iq_x x}dx\right]^2 \tag{A.15}$$

where L_x is the image pixels number per line, $h(x, y)$ represent the height values and q_x is the wave vector linked to x value of the height distribution. The PSD versus q curve, for self-affine surfaces, obeys a power law of the type:

$$\mathrm{PSD} = C_0 q^{-2-2H_c} \tag{A.16}$$

where H_c is defined as the image Hurst coefficient and C_0 is an arbitrary constant. The H_c is estimated by using the relation of the follow equation, where β is linearized curve declivity absolute value:

$$H_c = \frac{\beta - 2}{2} \tag{A.17}$$

SF method:

SF method is based on the structure function $S(\tau)$, one signal in a surface, $y(x)$ refers to the height of the signal, the relationship of $S(\tau)$ and the corresponding τ depends on D:

$$S(\tau) = \left\langle \left[y(x+\tau) - y(x)\right]^2 \right\rangle = \int_{-\infty}^{+\infty} S(\omega)(e^{j\omega\tau} - 1)\, d\omega = C\tau^{4-2D} \tag{A.18}$$

Given that each $S(\tau)$ and the corresponding τ, fitted in the double logarithmic coordinates, K is the of the slope of the curve, thus $D = (4 - K)/2, 0 < K < 2$, which is the dimension of this signal. Calculating all dimensions of the signals to get mean value $\overline{D}$, the dimension of the surface is $D_s = \overline{D} + 1$.

ACF method:

ACF method is based on the autocorrelation function $R(\tau)$, $y(x)$ refers to the hight of the signal, therefore:

$$R(\tau) = \langle y(x)y(x+\tau)\rangle \tag{A.19}$$

The relationship between the structure function $S(\tau)$ and the auto-correlation function $R(\tau)$ is:

$$S(\tau) = 2\left[R(0) - R(\tau)\right] \tag{A.20}$$

Thus its result is generally similar to the SF method.

RSE method:

Table A.1
Milling parameters.

State	Spindle speed (rpm)	Cutting depth (mm)	Feed rate (mm/min)
Stable	8000	15	1000
Chatter	6000	10	1000

RSE method used in surfaces is a little different from signals, the relevant calculation equations changed to:

$$Sq = AL^H = AL^{3-D} \tag{A.21}$$

$$\ln Sq = H \ln L + \ln A = (3 - D)\ln L + \ln A \tag{A.22}$$

A.2. Actual signals and surfaces

A.2.1. Milling vibration signals

Milling experiments were performed to obtain the vibration signals. The experiment setup is shown in Fig. A.1, a 5-axis numerical control machine tool (OUMA, DU810) was utilized, an accelerometer (ADI, ADXL345) was attached to the spindle to monitor the vibration and the signals were recorded with a data acquisition system (SIEMENS, LMSSCADASIII). An end milling tool with three blades (SWT, $\Phi 10 \times 30$ mm) was used to mill the top surface of the workpiece (Al 7075, $120 \times 120 \times 10$ mm).

During the experiments, the spindle rotated counterclockwise and the milling coordinate system is shown in Fig. A.1. The spindle moved in the X-axis direction at a uniform speed, and the vibration signal in the same direction was obtained. The pre-processing of vibration signals was the same as other signals used in our previous study. Plenty of the milling experiments under different cutting conditions were performed, two representative groups of signals were chosen to be investigated including stable vibration signals and chatter vibration signals, the cutting conditions are shown in Table A.1. The sampling frequency was 12 800 Hz for all experiments.

A.2.2. Thin films

The thin films were deposited on Si single crystal substrate by using a magnetron sputtering equipment. D was applied in many studies on thin films fabricated with physical vapor deposition methods including magnetron sputtering. The preparation process of the films was as follow: a silver target (diameter of 100 mm, thickness of 25 mm and purity of 99.99%) was selected to provide ions, P-type B-doped single crystal silicon (lattice orientation: ⟨100⟩, size: 15×15×0.5 mm, Rq: 1−10 nm) was the substrate. Within the environment (the initial vacuum pressure was

9×10^{-3} Pa, argon (Ar) was continuously injected to keep the pressure of 1.5 Pa, the sputtering power was 100 W) for 12 min, the substrate was sputtered. By adjusting the substrate temperature from 25–400 °C, a series of silver films with different surface morphologies were prepared, and atomic force microscopy (AFM, Bruker Dimension Icon, tapping mode) was employed to measure the morphological images, the sampling range was 2400 × 2400 nm. The typical images of silver thin film surfaces deposited via magnetron sputtering are shown in Figs. 3(b) and 5.

References

[1] Azpeitia E, Tichtinsky G, Le Masson M, Serrano-Mislata A, Lucas J, Gregis V, Gimenez C, Prunet N, Farcot E, Kater MM, Bradley D, Madueño F, Godin C, Parcy F. Cauliflower fractal forms arise from perturbations of floral gene networks. Science 2021;373(6551):192.

[2] Ramos GQ, Costa ICD, Costa MEHMD, Pinto EP, Matos RS, Filho HDF. Stereometric analysis of amazon rainforest Anacardium occidentale L. leaves. Planta 2021;253(1):6.

[3] Meyer HV, Dawes TJW, Serrani M, Bai W, Tokarczuk P, Cai J, de Marvao A, Henry A, Lumbers RT, Gierten J, Thumberger T, Wittbrodt J, Ware JS, Rueckert D, Matthews PM, Prasad SK, Costantino ML, Cook SA, Birney E, O'Regan DP. Genetic and functional insights into the fractal structure of the heart. Nature 2020;584(7822):589–94.

[4] Smyth PA, Rifkin RE, Jackson RL, Reid HR. The fractal structure of equine articular cartilage. Scanning 2012;34(6):418–26.

[5] Yan Y, Li X, Tang M, Zhong H, Huang J, Bian T, Jiang Y, Han Y, Zhang H, Yang D. Tailoring the edge sites of 2D Pd nanostructures with different fractal dimensions for enhanced electrocatalytic performance. Adv Sci 2018;5(8):1800430.

[6] Lanotte AS, Benzi R, Malapaka SK, Toschi F, Biferale L. Turbulence on a fractal Fourier set. Phys Rev Lett 2015;115(26):264502.

[7] Yang X, Liang YJ, Chen W. A fractal roughness model for the transport of fractional non-Newtonian fluid in microtubes. Chaos Solitons Fractals 2019;126:236–41.

[8] Mandelbrot BB. How long is the coast of britain? Statistical self-similarity and fractional dimension. Science 1967;156(3775):636–8.

[9] Mandelbrot BB. The fractal geometry of nature. New York: Freeman; 1983.

[10] Kenneth F. Fractal geometry: mathematical foundations and applications. Chichester: John Wiley & Sons; 1990.

[11] Paul M. Fractals, scaling and growth far from equilibrium. Cambridge: Cambridge University Press; 1998.

[12] Majumdar A, Tien CL. Fractal characterization and simulation of rough surfaces. Wear 1990;136(2):313–27.

[13] Yang ZY, Taghichian A, Huang GD. On the applicability of self-affinity concept in scale of three-dimensional rock joints. Int J Rock Mech Min 2011;48(7):1173–87.

[14] Lopes R, Betrouni N. Fractal and multifractal analysis: a review. Med Image Anal 2009;13(4):634–49.

[15] Wang SC, Zhang JF, Feng F, Qian X, Jiang LQ, Huang JL, Liu BB, Li J, Xia YS, Feng PF. Fractal analysis on artificial profiles and electroencephalography signals by roughness scaling extraction algorithm. IEEE Access 2019;7:89265–77.

[16] Jun Y, Yoon Y, Yoon H. ECG data compression using fractal interpolation. In: Proc 16th Int Conf IEEE Eng Med Biol Soc, Vol. 1; 1994, p. 161–2.

[17] Xu CW, Chen HL, Liu Z, W. CZ. Condition monitoring of milling tool wear based on fractal dimension of vibration signals. Stroj Vestn: J Mech E 2009;55:15–25.

[18] Ji YJ, Wang XB, Liu ZB, Yan ZH, Jiao L, Wang DQ, Wang JQ. EEMD-based online milling chatter detection by fractal dimension and power spectral entropy. Int J Adv Manuf Technol 2017;92(1–4):1185–200.

[19] Pang Y, Feng P, Wang J, Zha H, Xu J. Performance analysis of the longitudinal-torsional ultrasonic milling of Ti-6Al-4V. Int J Adv Manuf Technol 2021;113(5–6):1255–66.

[20] Zhou WM, Cao YT, Zhao HL, Li ZW, Feng PF, Feng F. Fractal analysis on surface topography of thin films: A review. Fractal Fract 2022;6:135.

[21] Catalan G, Bea H, Fusil S, Bibes M, Paruch P, Barthelemy A, Scott JF. Fractal dimension and size scaling of domains in thin films of multiferroic BiFeO3. Phys Rev Lett 2008;100(2):027602.

[22] Marques IHG, Saraiva MR, Yonny RB, lu S, Moreira JA, Almeida A, Cruz JPD, Filho HDF. Investigation of stereometric and fractal patterns of spin-coated LuMnO3 thin films. Adv Mater Sci Eng 2021;2021:1–11.

[23] Yonny RB, Matos RS, Pedra̧ ca AS, Cruz JPD, Brito WR, Oliveira RMPB, Filho HDF. Advanced spatial investigation of 3D nanoscale topography of DyMnO3 thin films. Physica B 2021;623.

[24] Das A, Matos RS, Pinto EP, Yadav RP, lu S, Kumar S. 3D micromorphology-contact resistance-conductivity insights of quasi 2D Cd1-xPbxS thin films: Investigation based on stereometric and fractal analysis. Mater Chem Phys 2022;278.

[25] Peitgen HO, Jürgens H, Saupe D. Chaos and fractals: new frontiers of science. 2nd ed.. New York: Springer Verlag; 2004.

[26] Ai T, Zhang R, Zhou HW, Pei JL. Box-counting methods to directly estimate the fractal dimension of a rock surface. Appl Surf Sci 2014;314:610–21.

[27] Pinto EP, Pires MA, Matos RS, Zamora RRM, Menezes RP, Araújo RS, Souza TMD. Lacunarity exponent and moran index: A complementary methodology to analyze AFM images and its application to chitosan films. Physica A 2021;581.

[28] Higuchi T. Approach to an irregular time series on the basis of the fractal theory. Physica D 1988;31(2):277–83.

[29] Katz MJ. Fractals and the analysis of waveforms. Comput Biol Med 1988;18(3):145–56.

[30] Jacobs TDB, Junge T, Pastewka L. Quantitative characterization of surface topography using spectral analysis. Surf Topogr-Metrol 2017;5(1).

[31] Wu JJ. Analyses and simulation of anisotropic fractal surfaces. Chaos Solitons Fractals 2002;13(9):1791–806.

[32] Sayles RS, Thomas TR. The spatial representation of surface roughness by means of the structure function: A practical alternative to correlation. Wear 1977;42(2):263–76.

[33] Li ZW, Qian X, Feng F, Qu TM, Xia YS, Zhou WM. A continuous variation of roughness scaling characteristics across fractal and non-fractal profiles. Fractals 2021;29(5):2150109.

[34] Feng F, Liu BB, Zhang XS, Qian X, Li XH, Huang JL, Qu TM, Feng PF. Roughness scaling extraction method for fractal dimension evaluation based on a single morphological image. Appl Surf Sci 2018;458:489–94.

[35] Wong PCY, Kwon YN, Criddle CS. Use of atomic force microscopy and fractal geometry to characterize the roughness of nano-, micro-, and ultrafiltration membranes. J Membr Sci 2009;340(1–2):117–32.

[36] Malinverno A. A simple method to estimate the fractal dimension of a self-affine series. Geophys Res Lett 1990;17(11):1953–6.

[37] Chauvy PF, Madore C, Landolt D. Variable length scale analysis of surface topography: characterization of titanium surfaces for biomedical applications. Surf Coat Technol 1998;110(1):48–56.

[38] Zhang XH, Jackson RL. An analysis of the multiscale structure of surfaces with various finishes. Tribol T 2016;60(1):121–34.

[39] Zhang XH, Xu Y, Jackson RL. An analysis of generated fractal and measured rough surfaces in regards to their multi-scale structure and fractal dimension. Tribol Int 2017;105:94–101.

[40] Chen ZY, Liu Y, Zhou P. A comparative study of fractal dimension calculation methods for rough surface profiles. Chaos Solitons Fractals 2018;112:24–30.

[41] Albuquerque MDDFD, Simão RA, Matos RS, Pinto EP, Pires MA, Filho HDDF, de Mello MBDM. Nanoscale stereometric and fractal evaluation of clathrate formation at quartz surface by atomic force microscopy. Miner Eng 2021;170.

[42] Oliveira LMD, Matos RS, Talu S, Rocha ALF, Nunes RZDA, Bezerra JA, Felix PHC, Inada NM, Sanches EA, Filho HDF. Three-dimensional nanoscale morphological surface analysis of polymeric particles containing allium sativum essential oil. Materials 2022;15(7).

[43] Feng F, Huang JL, Li XH, Qu TM, Liu BB, Zhou WM, Qian X, Feng PF. Influences of planarization modification and morphological filtering by AFM probe-tip on the evaluation accuracy of fractal dimension. Surf Coat Technol 2019;363:436–41.

[44] Jarnicki M, Pflug P. Continuous nowhere differentiable functions. Cham, Switzerland: Springer; 2015.

[45] Berry MV, Lewis ZV, Nye JF. On the weierstrass-mandelbrot fractal function. Proc R Soc Lond Ser A Math Phys Eng Sci 1980;370(1743):459–84.

[46] Chen ZY, Liu Y, Zhou P. A comparative study of fractal dimension calculation methods for rough surface profiles. Chaos Solitons Fractals 2018;112:24–30.

[47] Zuo X, Tang X, Zhou YK. Influence of sampling length on estimated fractal dimension of surface profile. Chaos Solitons Fractals 2020;135.

[48] Yao K, Chen HT, Peng WL, Wang ZK, Yao J, Wu YP. A new method on box dimension of weyl-marchaud fractional derivative of Weierstrass function. Chaos Solitons Fractals 2021;142.

[49] Kulesza S, Bramowicz M. A comparative study of correlation methods for determination of fractal parameters in surface characterization. Appl Surf Sci 2014;293:196–201.

[50] Liu Y, Wang YS, Chen X, Yu HC. A spherical conformal contact model considering frictional and microscopic factors based on fractal theory. Chaos Solitons Fractals 2018;111:96–107.

[51] Ausloos M, Berman DH. A multivariate weierstrass–mandelbrot function. Proc R Soc Lond Ser A Math Phys Eng Sci 1997;400(1819):331–50.

[52] Takagi T. A simple example of a continuous function without derivative. Proc Phys Math Soc Jpn 1903;1.

[53] Hata M, Yamaguti M. The takagi function and its generalization. Jpn J Appl Math 1984;1(1):183–99.

[54] Kulatilake PHSW, Um J. Requirements for accurate quantification of self-affine roughness using the roughness–length method. Int J Rock Mech Min 1999;36(1):5–18.

[55] Kulatilake PHSW, Um J, Pan G. Requirements for accurate estimation of fractal parameters for self-affine roughness profiles using the line scaling method. Rock Mech Rock Eng 1997;30(4):181–206.

[56] Wan SK, Li XH, Yin YJ, Hong J. Milling chatter detection by multi-feature fusion and adaboost-SVM. Mech Syst Signal Proc 2021;156.

[57] Mishra R, Singh B. Stability analysis in milling process using spline based local mean decomposition (SBLMD) technique and statistical indicators. Measurement 2021;174.
[58] Zhu LD, Liu CF. Recent progress of chatter prediction, detection and suppression in milling. Mech Syst Signal Proc 2020;143.
[59] Li XH, Wan SK, Huang XW, Hong J. Milling chatter detection based on VMD and difference of power spectral entropy. Int J Adv Manuf Technol 2020;111(7–8):2051–63.
[60] Li K, He SP, Li B, Liu HQ, Mao XY, Shi CM. A novel online chatter detection method in milling process based on multiscale entropy and gradient tree boosting. Mech Syst Signal Proc 2020;135.
[61] Ji YJ, Wang XB, Liu ZB, Wang HJ, Jiao L, Wang DQ, Leng SY. Early milling chatter identification by improved empirical mode decomposition and multi-indicator synthetic evaluation. J Sound Vib 2018;433:138–59.
[62] Wan M, Dang XB, Zhang WH, Yang Y. Chatter suppression in the milling process of the weakly-rigid workpiece through a moving fixture. J Mater Process Technol 2021;299:117293.
[63] Pan YQ, Wu ZS, Hang LX. Influence of ag thin films on surface roughness and light scattering of optical substrate. Acta Photon Sin 2009;38:1197–201.
[64] Conceição WSD, Matos RS, Melo IDC, Ramos GQ, Zayas FG, Filho HDF. Measurement of wood surface roughness in dinizia excelsa ducke using an atomic force microscope. Acta Sci Technol 2022;44.
[65] Ghribi F, Khalifi N, Mrabet S, Ghiloufi I, lu S, El MLM, Filho HDF, Oliveira RMPB, Matos RS. Evaluation of the structure–micromorphology relationship of Co10 nanostructured thin films deposited by pulsed laser using XRD and AFM. Arab J Sci Eng 2022;47(6):7717–28.
[66] Gandarilla AMD, Matos RS, Barcelay YR, Filho HDF, Brito WR. Molecularly imprinted polymer on indium tin oxide substrate for bovine serum albumin determination. J Polym Res 2022;29(5).
[67] Zhuo Y, Jin HY, Han ZY. Chatter identification in flank milling of thin-walled blade based on fractal dimension. Procedia Manuf 2020;49:150–4.
[68] Chen Y, Li HZ, Hou L, Bu XJ, Ye SG, Chen D. Chatter detection for milling using novel p-leader multifractal features. J Intell Manuf 2022;33(1):121–35.
[69] Jing XB, Zheng ZH, Xu J, Wang FJ, Jaffery SHI, Li HZ. Stability analysis in micro milling based on p-leader multifractal method. J Manuf Process 2022;77:495–507.
[70] Zhou G, Wang XH, Feng F, Feng PF, Zhang M. Calculation of fractal dimension based on artificial neural network and its application for machined surfaces. Fractals 2021;2150129.
[71] Talu S, Monteiro MDS, Filho HDF, Ferreira NS, Matos RS. Surface aspects and multifractal features of 3D spatial patterns of low-cost amazon acai-loaded kefir microbial films. Microsc Res Technol 2022;85(7):2526–36.